

TRANSITION OF SEPARATED FLOW OVER A BUMP UNDER UNSTEADY INFLOW CONDITIONS

HIMPU MARBONA^{1,2,*}, ALEJANDRO MARTÍNEZ-CAVA^{1,3}, DANIEL
RODRÍGUEZ^{1,2}, AND EUSEBIO VALERO^{1,2}

¹ Universidad Politécnica de Madrid, Plaza Cardenal Cisneros 3, E-28040 Madrid, Spain

²Center for Computational Simulation, Universidad Politécnica de Madrid, Campus de Montegancedo, Boadilla del Monte, 28660 Madrid, Spain

³Instituto Universitario “Ignacio Da Riva” (IDR/UPM), Universidad Politécnica de Madrid, Plaza Cardenal Cisneros, 3, E-28040, Madrid, Spain

*Corresponding author. E-mail address: himpu.marbona@upm.es

Key words: Separated flow, laminar-turbulent transition, hydrodynamic instability, direct numerical simulation, low-pressure turbines

Abstract. Laminar flow separation has detrimental effects on the aerodynamics and performance of low pressure turbines (LPT). Flow separation is caused by the presence of adverse pressure gradient condition on the upper side of the blade past the suction peak, and is followed by laminar-to-turbulent transition and the subsequent turbulent mean reattachment due to the enhanced mixing. These phenomena characterise the size and dynamics of the separated flow, which are primarily dominated by the laminar-turbulent process. This study examines the influence of periodically-varying inflow conditions on the separated flow over a bump geometry at low Reynolds numbers. The geometry and flow conditions represent the upper surface of small LPT during high-altitude of flight. Direct numerical simulations are performed, in which a harmonic variation of the inlet total pressure is imposed, as a rough approximation of the passage of the upstream blade’s wake. Three different frequencies with identical amplitude of the total pressure are simulated. The dynamics of the separated shear layer and the transition process are studied by separating the flow components correlated and un-correlated to the inflow frequency. Even moderate frequencies are found to have a strong effect in reducing the averaged size of the separated flow region, thus reducing the losses.

1 INTRODUCTION

Boundary layer separation on laminar flow is a ubiquitous phenomenon present in several aeronautical applications, such as low-pressure turbines (LPT) at high-altitude flight [1, 2] and Unmanned Aerial Vehicle (UAV) or Micro Aerial Vehicle (MAV) wings [3]. Separated flow is associated with detrimental effects on the aerodynamics and performance at which flow control strategies that lead to reductions in the size of the separated flow region are a way forward towards improving their efficiency [4]. Following from the laminar separation, the laminar-to-turbulent transition process has a dominant role in the reattachment of the separated flow,

thus determining the extent and dynamics of separation bubbles [2,5,6]. This transition process also impacts the structural loading of LPT blades [5]. The details of the transition process in separated flows and the underlying hydrodynamic instabilities are relatively well known when the incoming flow and the aerodynamic surface are under steady conditions [6–8]. However, the impact of temporal variations of the incoming flow on the whole process has received less attention. Such variations occur naturally in LPTs as a result of the periodic passage of the wake of one blade row over the blades of the subsequent row, and can modify the mean flow properties in a relevant manner [9].

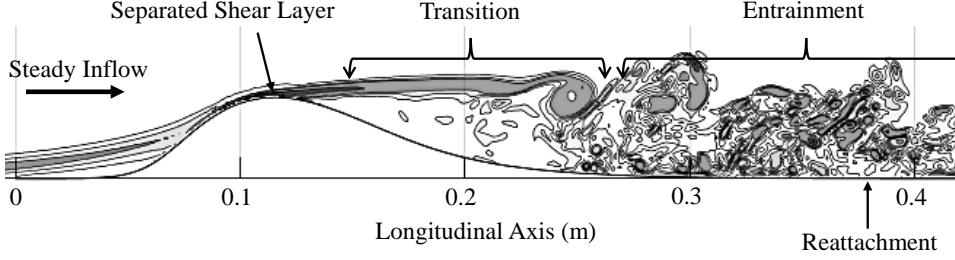


Figure 1: Spanwise vorticity downstream of a bump under steady inflow

This work studies the laminar separation bubble formed over a wall-mounted bump geometry that reproduces some characteristics of the suction side of an LPT blade. Similar geometries have been employed in the past both experimentally and numerically to study the fundamental physics of the separated flow [7, 10–12]. Figure 1 illustrates the flow configuration. Under a steady inflow, the laminar boundary layer separates just downstream of the bump summit, where it encounters the adverse pressure gradient. The separated shear layer sustains the self-excited shedding of spanwise-dominant vortices, which is followed by an abrupt transition to turbulence. The intense entrainment provided by turbulence leads to the mean flow reattachment [10]. The time-dependent changes in the inflow conditions can influence the dynamics strongly. Numerical and experimental works on the same geometry have demonstrated a reduction in the size of the separated flow region when subjected to flow acceleration and an increase in the bubble size during deceleration [11]. Another experimental study [12], considering a sudden flow release, showed the absence of flow separation as indicated by the non-existence of a plateau in the pressure distribution, reproduced in figure 2.

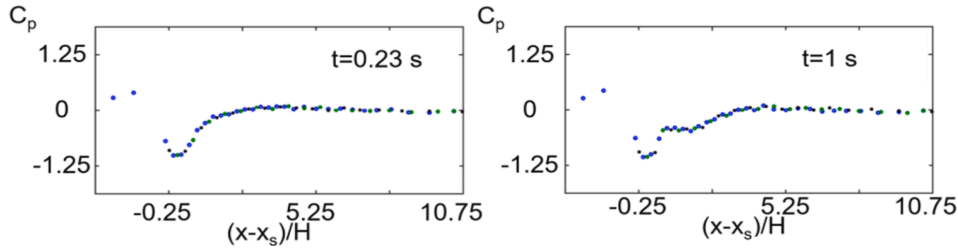


Figure 2: Pressure over a bump under sudden flow release; accelerating (left) and steady (right)[12]

Four inlet conditions are considered in this work. The first one is a steady inflow prescribed

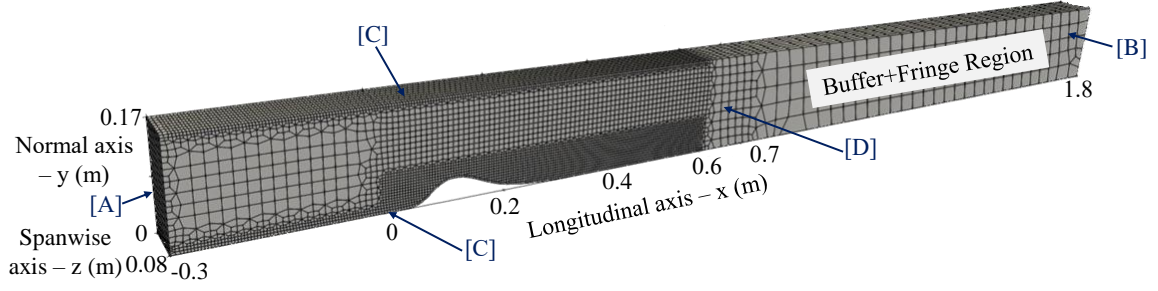


Figure 3: Numerical domain and mesh

by a constant pressure difference between the inflow and outflow that results in the transition scenario shown in figure 1. For this case, the Reynolds number based on the mean velocity and the reference length $L^* = 0.1\text{m}$ is 10,000 and the Mach number is 0.2. The other three inlet conditions consist on a harmonic variation of the inlet total pressure, to represent the effect of the passage of the previous blade's wake. Three different frequencies are prescribed, that illustrate how the laminar-to-turbulent process is altered on account of the periodic flow.

2 NUMERICAL APPROACH

Table 1: Boundary Conditions

[A] Inlet	Total Pressure and Temperature
[B] Outlet	Static Pressure: 101325 Pa
[C] Wall	No-Slip Wall, Adiabatic 15°C
[D] Sides	Periodic

The computational domain and discretisation mesh used are shown in figure 3. With the aim of reproducing the experimental set up by Saavedra *et al.* [11, 12], the same geometry comprising a plane channel with a bump is used. The bump is defined by Bezier curves to ensure continuity of the surface up to the second derivatives. The bump maximum height (summit) and the channel's height are respectively 0.036m and 0.17m. Further details on the definition of the bump can be found in [11, 12]. In the present computations, the channel is considered to be homogeneous in the spanwise direction. The spanwise size of the computational domain is set as 0.08m (more than twice the bump height), and periodic boundary conditions are imposed on the lateral walls. The computational domain is extended along the streamwise direction with respect to the reference experiments and simulations to minimise the impact of the boundary conditions. The inlet section [A] is located 0.3m upstream of the beginning of the bump; uniform values of total pressure and temperature are imposed in this section. Consequently, velocity distributions that satisfy the boundary conditions will be obtained as part of the solution, but are not directly imposed. The relatively long distance between the inlet section and the bump is intended to allow for the development of the boundary layer. A uniform static pressure

value is imposed at the outlet section [B]. Preliminary calculations showed that the outflow boundary can generate acoustic reflections and other sources of spurious upstream influence, contaminating the solution in the separated flow region. To minimise this influence, a very long domain was used to accommodate a buffer/fringe region, that starts in $x = 0.7\text{m}$ and extends up to $x = 1.8\text{m}$. The discretising elements are intentionally coarse in this region to facilitate that the increased numerical dissipation dampens the flow fluctuations as they are advected. In addition, volumetric source terms are applied in this region to force the flow to damp any fluctuations [13]. Adiabatic and no-slip conditions are imposed to the top and bottom walls. The boundary conditions are summarised in table 1.

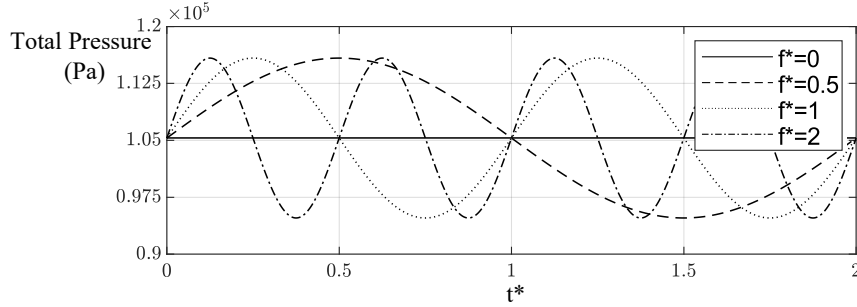


Figure 4: Inlet total pressure

The flow is driven by the pressure gradient imposed via the inflow and outflow boundary conditions. Four cases are considered. The first case, referred to as *steady* inflow, imposes a constant value of the inlet total pressure. In the other three cases, a harmonic variation of the total pressure is prescribed upon the value imposed to the steady inflow case, as shown in figure 4. The amplitude of the total pressure oscillation is the same in all cases, and three different dimensionless frequencies are imposed: $f^* = 0.5, 1$ and 2 . The dimensionless form used is discussed next.

Throughout this work the lengths are presented in a dimensional manner to allow for comparison with the reference experiment and simulations. A reference length $L^* = 0.1\text{m}$ is introduced as representative of the chord of an LPT blade “embedded” in the bump geometry. The mean velocity at the inflow section for the steady inflow case, $U_{ref} = 68.158\text{ m/s}$, is taken as reference for the velocity, resulting in the Reynolds number

$$Re = \frac{U_{ref}L^*}{\nu} \approx 10,000. \quad (1)$$

Time is scaled using U_{ref} and the unit length

$$t^* = \frac{t U_{ref}}{1 [m]}, \quad (2)$$

resulting in the dimensionless frequency

$$f^* = \frac{1}{t^*}. \quad (3)$$

Direct numerical simulations are performed using the in-house discontinuous Galerkin spectral element code HORSES3D [14]. The particularities of high-order methods regarding accuracy and numerical stability result in different requirements for the computational mesh than low-order methods most extended in computational fluid dynamics like finite volumes or finite differences. Figure 3 illustrates the mesh finally used in the simulations; this mesh is the result of a mesh convergence study that is not reported here for brevity. The final mesh consist of 32,000 rectangular elements on the streamwise plane with 8 elements in the spanwise z -direction.

HORSES3D solves the compressible Navier-Stokes equations in conservative form [14]:

$$\frac{\partial \mathbf{q}}{\partial t} + \vec{\nabla} \cdot (\vec{\mathbf{f}}^a - \vec{\mathbf{f}}^v) = \mathbf{s} \quad (4)$$

where $\mathbf{q} = [\rho, \rho u, \rho v, \rho w, \rho E]^T$ are the conservative variables and \mathbf{s} is a source or volumetric forcing term. Advection ($\vec{\mathbf{f}}^a$) and viscous ($\vec{\mathbf{f}}^v$) fluxes are expressed in primitive variables as (5) and (6), respectively.

$$\mathbf{f}_1^a = \begin{bmatrix} \rho u \\ p + \rho u^2 \\ \rho uv \\ \rho uw \\ u(\rho E + p) \end{bmatrix}, \quad \mathbf{f}_2^a = \begin{bmatrix} \rho v \\ \rho vw \\ p + \rho v^2 \\ \rho vw \\ v(\rho E + p) \end{bmatrix}, \quad \mathbf{f}_3^a = \begin{bmatrix} \rho w \\ \rho uw \\ \rho vw \\ p + \rho w^2 \\ w(\rho E + p) \end{bmatrix} \quad (5)$$

$$\mathbf{f}_1^v = \begin{bmatrix} 0 \\ \tau_{xx} \\ \tau_{xy} \\ \tau_{xz} \\ v_i \tau_{1i} + \kappa \partial_x T \end{bmatrix}, \quad \mathbf{f}_2^v = \begin{bmatrix} 0 \\ \tau_{yx} \\ \tau_{yy} \\ \tau_{yz} \\ v_i \tau_{2i} + \kappa \partial_y T \end{bmatrix}, \quad \mathbf{f}_3^v = \begin{bmatrix} 0 \\ \tau_{zx} \\ \tau_{zy} \\ \tau_{zz} \\ v_i \tau_{3i} + \kappa \partial_z T \end{bmatrix} \quad (6)$$

All the simulations presented herein are performed using 3rd-order polynomials. Time integration is performed with an explicit 3rd-order Runge-Kutta scheme. A standard discontinuous Galerkin discretisation of the inviscid fluxes is done using Roe's method for the Riemann problem. The Bassi-Rebay 1 scheme is used for the discretisation of the viscous fluxes.

3 RESULTS

Figure 5 shows the instantaneous spanwise vorticity fields at different time instants for the case with $f^* = 0.5$. In addition to the dimensionless time, each subfigure also indicates the corresponding phase ϕ of the inflow total pressure at $x = 0\text{m}$. For $\phi = 0^\circ$ the inflow total pressure starts to increase above the mean value, exerting an acceleration of the flow along the channel. Due to the increased mass and momentum fluxes, the separated shear layer is pushed towards the bump wall. Vortex shedding from the aft part of the shear layer is visible, that develops into a turbulent region shortly downstream. As the flow is accelerated, the high vorticity region associated with the turbulent transition is also pushed towards the wall. The maximum inflow pressure occurs at $\phi = 90^\circ$. For ϕ between 90° and 270° the inflow pressure is reduced up to its minimum value, imposing a gradual deceleration of the bulk flow. The separated shear layer moves away from the wall; the high vorticity region seems to detach from the wall and the

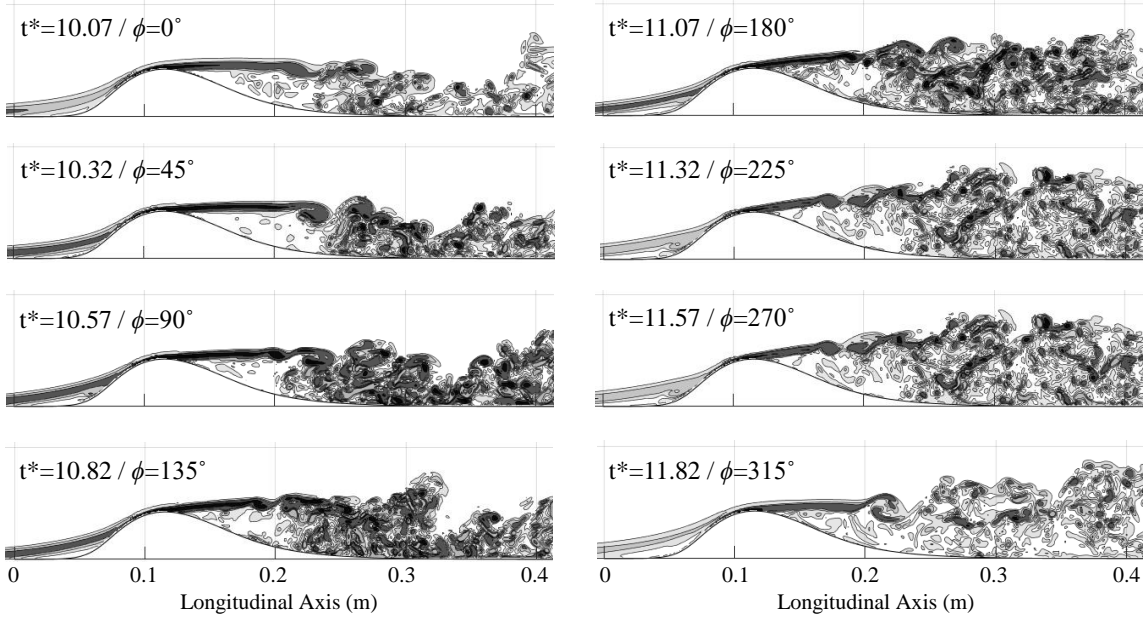


Figure 5: Instantaneous results of spanwise vorticity - $f^*=0.5$

apparent recirculation region extends farther in the streamwise direction. Finally, for $\phi > 270^\circ$ the flow gradually re-accelerates closing the period.

These observations suggest that two closely related but different physical mechanisms are at play when the inflow has a harmonic time dependence. First, the periodic acceleration and deceleration of the bulk flow modifies the angle of the separated shear layer through changes in the intensity of the streamwise pressure gradient. The location of the separation point is nearly unaffected by this. Second, the periodic motion of the shear layer impacts its hydrodynamic instability properties, and subsequently the vortex shedding process and the details of the laminar-turbulent transition. The streamwise extent of the separated flow is ultimately determined by the combination of both.

The analysis presented in what follows attempts to isolate the two dynamics by applying the triple decomposition proposed by Hussain & Reynolds [15]:

$$\mathbf{q}(\mathbf{x}, t) = \bar{\mathbf{q}}(\mathbf{x}) + \tilde{\mathbf{q}}(\mathbf{x}, t) + \mathbf{q}'(\mathbf{x}, t), \quad (7)$$

where $\bar{\mathbf{q}}$ stands for the mean (i.e. time-averaged) flow, $\tilde{\mathbf{q}}$ is the phase-averaged (or correlated) *oscillatory* component and \mathbf{q}' is the un-correlated flow component. This decomposition is intended here to separate the flow oscillations that are in phase with the harmonic inflow acceleration/deceleration - the motion of the separated of the shear layer - from the vortex shedding and evolution. As such, the mean and correlated oscillation components are gathered together in the phase-averaged flow

$$\langle \mathbf{q}(\mathbf{x}, \phi) \rangle = \frac{1}{N} \sum_{n=0}^N \mathbf{q} \left(\mathbf{x}, t_\phi + \frac{n}{f^*} \right), \quad (8)$$

where t_ϕ is the time used as phase reference, f^* is the inlet frequency and N is the number of periods used in the averaging. The uncorrelated part of the flow is computed as $\mathbf{q}'(\mathbf{x}, \mathbf{t}) = \mathbf{q}(\mathbf{x}, \mathbf{t}) - \langle \mathbf{q}(\mathbf{x}, \mathbf{t}) \rangle$. The same dimensionless time lapse was used in the averaging for the three frequencies f^* , corresponding to $N = 20$ for $f^* = 0.5$, $N = 40$ for $f^* = 1$ and $N = 80$ for $f^* = 2$. The data corresponding to the initial transient after the initialisation of the simulation was discarded.

3.1 Phase-averaged flow

Figure 6 shows the phase-averaged spanwise vorticity fields for phases $\phi = 0^\circ, 90^\circ, 180^\circ$ and 270° for the case $f^* = 0.5$. For this case, the phase-averaging is able to separate the shear-layer motion from the vortex shedding and transition. Following the harmonic acceleration and deceleration of the bulk flow imposed by the inflow condition, the angle of the separated shear layer oscillates, moving the phase-averaged separation streamline (shown as a dark solid line in the figure) apart and towards the wall. The changes in the separated shear layer impact the hydrodynamic instability properties [6, 16] and consequently the complete process of laminar-to-turbulent transition and reattachment. While the phase-averaging filters out these dynamics, it effectively captures the periodic change in the size of the separation bubble.

The streamwise length of the recirculation bubble is computed at each phase ϕ as the distance between the location where the streamwise wall shear τ_w changes from positive to negative near the bump summit (the separation point) and the first point downstream where it changes from negative to positive. Figure 7 shows the probability density function of the recirculation length for the three inflow frequencies. The mean length for each case is shown as a vertical dashed line and the dash-dotted line is the mean value for the case with steady inflow. The mean length is significantly reduced as f^* is increased. For $f^* = 0.5$ and 1 the PDF is relatively broad, suggesting that the impact of the shear layer oscillation on the transition process involves qualitative changes along the period. Both cases present a peak around 0.3, considerably longer than the mean value, which is likely to be associated with the part of the period following the peak deceleration. For $f^* = 2$ the PDF is narrower and centred around the mean value.

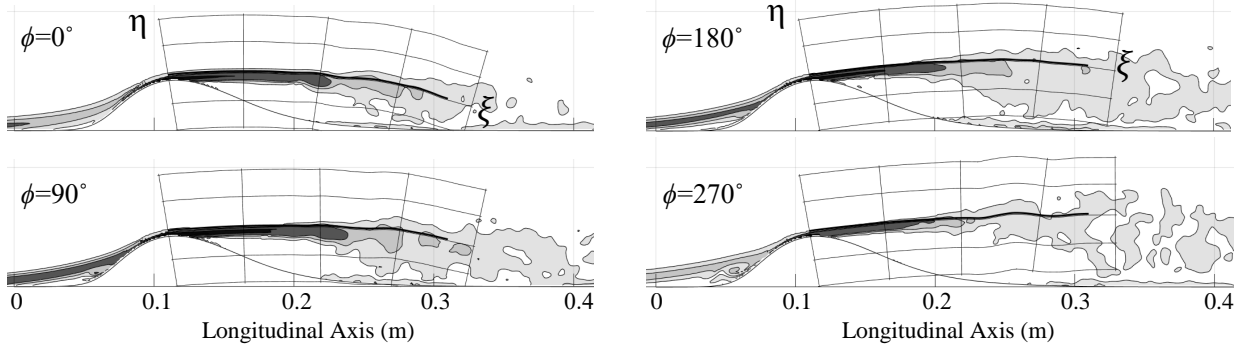


Figure 6: Phase average of spanwise vorticity - $f^*=0.5$

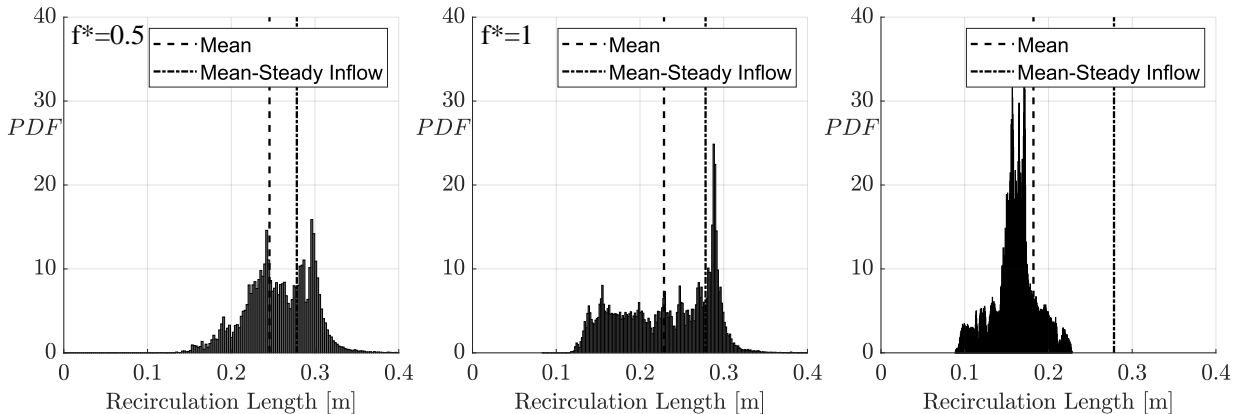


Figure 7: Probability density function of the recirculation bubble length for different inflow frequencies.

3.2 Vortex dynamics and transition

The impact of the inflow frequency on the length of the recirculation region is a consequence of changes in the vortex dynamics induced by the motion of the shear layer. Resulting from the Kelvin-Helmholtz instability, vortex rolls are formed at the separated shear layer that initiate the laminar-to-turbulent transition. For low f^* , the characteristic period in which the shear-layer motion occurs is much longer than the characteristic time for the formation and advection of the vortices. In consequence, the vortex dynamics are completely recovered in the un-correlated flow component \mathbf{q}' of the triple decomposition. The vortices are formed and initially move along the separated shear layer, whose motion is captured by the phase-averaged component.

To separate the vortex dynamics from the shear layer motion, the following procedure is followed. First, an orthogonal curvilinear coordinate system (ξ, η) is defined, based on the phase-averaged field. The coordinate line $\eta = 0$ corresponds to the (instantaneous) streamline departing from the separation point, with ξ being the arc length. Coordinate η measures the normal distance from the separation streamline at each point. This *shear-layer fitted* system of coordinates is inspired by the one used in [17] to study the vortex dynamics along the *steady* shear layer formed within a slat cove. In the present case, the curvilinear coordinates depend on the phase angle, following the motion of the phase-averaged separation streamline. The curvilinear coordinates are shown in figure 6.

Figure 8 shows the total (left column), the phase-averaged (middle column) and the uncorrelated (right column) components of the spanwise vorticity in the curvilinear mesh. Note that the bump wall appears as a curve line for $\eta < 0$ whose geometry changes with the phase. As expected, the phase-averaged shear layer corresponds approximately to the horizontal line $\eta = 0$. The uncorrelated component portrays a complex arrangement of vortical structures typical of turbulent flow. However, the process is initiated with the formation of pockets of vorticity in the initial part of the shear layer, at comparatively small amplitudes. To visualise the spatio-temporal dynamics of these vortices, the uncorrelated spanwise vorticity ω'_z at $\eta = 0$ is plotted in the (ξ, t^*) plane in figure 9.

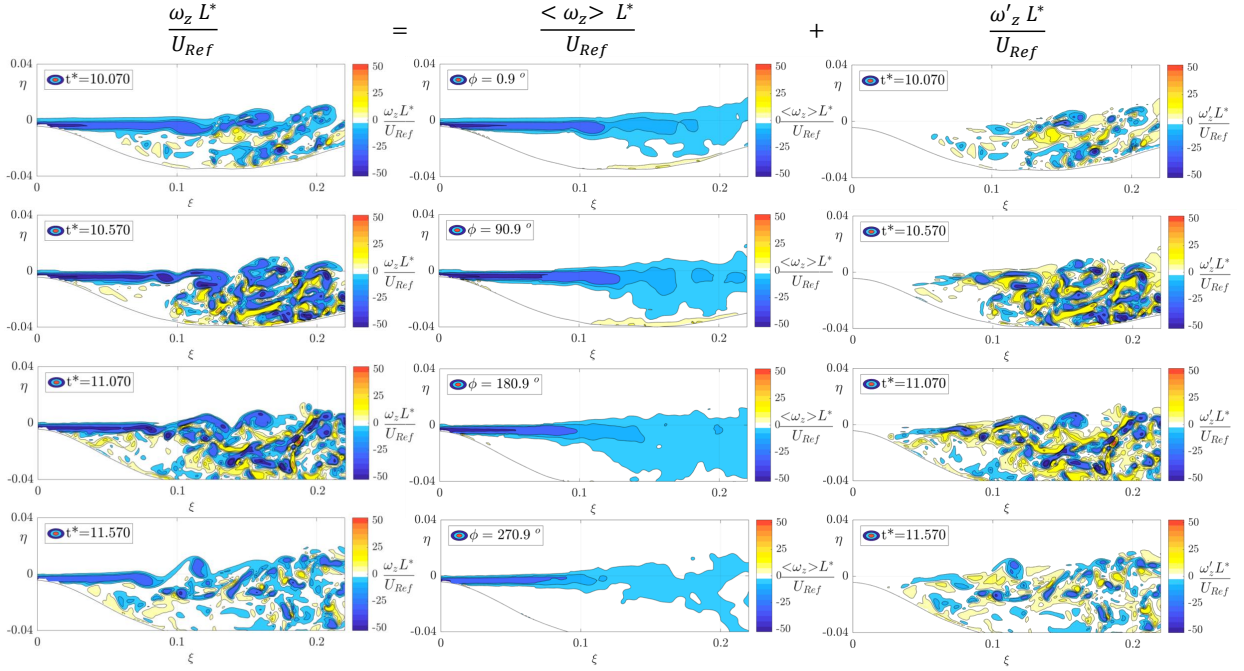


Figure 8: Triple decomposition of spanwise vorticity - $f^*=0.5$

The left panel in Fig. 9 corresponds to $f^* = 0.5$ and one complete inflow period is shown. The dark blue streaks correspond to the formation and advection of vortices. The temporal delay between vortices T_v is relatively constant over the inflow period and much shorter than it ($T_v \ll T^* = 1/f^*$). Conversely, the ξ coordinate in which the uncorrelated vorticity reaches nonlinear amplitudes and becomes observable (with the present choice of contour levels) varies following the inflow phase. This variation is not sinusoidal, suggesting hysteresis effects specially during the acceleration phase (e.g. from $t^* = 7.25$ to 8 in the figure). The hysteresis effect is more notable for $f^* = 1$ (e.g. $t^* = 10.75$ to 11.25). During this time lapse, the organised streaks typical of the uncorrelated vortex shedding are replaced by a clearly different structure, that reaches nonlinear amplitudes a shorter distance from $\xi = 0$. These structures are not truly uncorrelated with the harmonic inflow changes, and correspond to large vortex clusters being formed and swept downstream during the accelerating phase. Finally, the right panel of figure 9 corresponds to $f^* = 2$. In this case the vortex dynamics are completely dominated by the periodic formation of large vortex clusters on account of the inflow changes. Observable, nonlinear amplitudes are present well upstream compared to the other two cases, indicating an earlier transition to turbulence which is consistent with the reduced recirculation lengths observed in figure 7.

4 CONCLUSIONS

The dynamics of the separated shear layer and the laminar-to-turbulent transition occurring in the laminar separation bubble formed past a bump under unsteady inflow conditions are

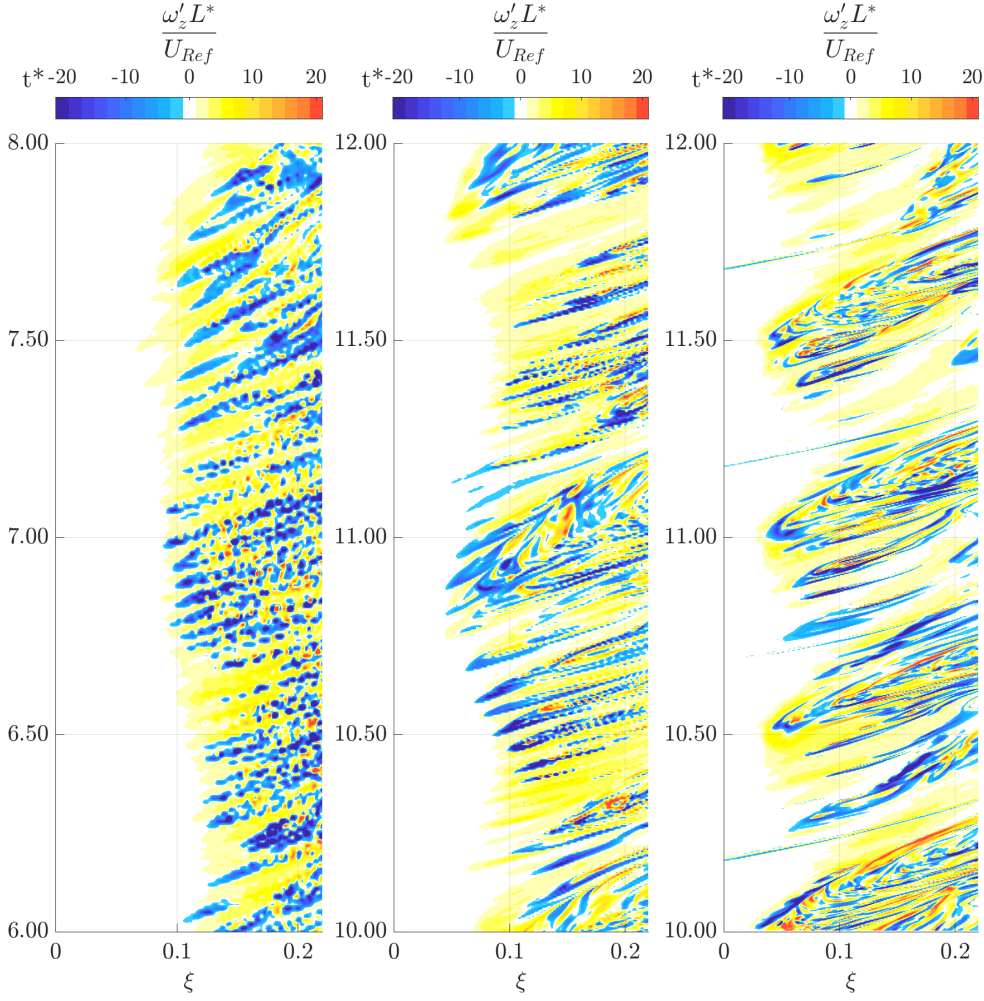


Figure 9: Uncorrelated spanwise vorticity at $\eta=0$ - $f^*=0.5,1,2$ (left to right)

studied using direct numerical simulations. The inflow total pressure is varied harmonically about a reference value, exerting a periodic acceleration and deceleration of the bulk flow. The separated flow dynamics are impacted through two related mechanisms. First, the periodic change in the bulk flow induces a vertical motion of the separated shear layer towards and away from the bump wall. Second, this changes alter the vortex dynamics and the transition process. The transition for relatively low frequencies seems to be dominated by the vortex shedding sustained by the shear layer. As the inflow frequency is increased, the faster displacement of the shear layer gives rise to large vortex clusters that are advected downstream during the acceleration part of the period. The net effect is a notable reduction of the recirculation flow length for the highest frequency considered.

ACKNOWLEDGMENTS

This project has received funding from the European Union's Horizon 2020 research and

innovation programme under the Marie Skłodowska Curie grant agreements No 101019137-FLOWCID and 955923-SSECOID. D.R. also acknowledges funding by the Government of the Community of Madrid within the multi-annual agreement with Universidad Politécnica de Madrid through the Program of Excellence in Faculty (V-PRICIT line 3).

The authors gratefully acknowledge the Universidad Politécnica de Madrid (www.upm.es) for providing computing resources on Magerit Supercomputer.

REFERENCES

- [1] Bons J.P, Sondergaard R and Rivir R.B. The fluid dynamics of LPT blade separation control using pulsed jets. *ASME J. Turbomach.*, Vol. 124(1), pp. 77-85. 2002.
- [2] Mayle R.E. The role of laminar-turbulent transition in gas turbine engines. *ASME J. Turbomach.*, Vol. 113, pp. 509–536. 1991.
- [3] Visbal, M. Unsteady low Reynolds number aerodynamics for micro air vehicles (MAVs). Air Force Research Laboratory. AFRL-RB-WP-TR-2010-3013. 2010.
- [4] Volino R.J, Kartuzova O and Ibrahim M.B. Separation control on a very high lift low pressure turbine airfoil using pulsed vortex generator jets. *ASME J. Turbomach.*, 0889-504X, 133(4), p. 041021. 2011.
- [5] Curtis E. M., Hodson H. P., Banieghbal M. R., Denton J. D., Howell R. J., and Harvey N. W. Development of blade profiles for low-pressure turbine applications. *ASME J. Turbomach.*, Vol. 119, pp. 531–538. 1997.
- [6] Dovgal A.V, Kozlov V.V and Michalke A. Laminar boundary layer separation: instability and associated phenomena. *Prog. Aerospace Sci.*, Vol. 30, pp.61-94, 1994.
- [7] Passaggia P.Y, Leweke T and Ehrenstein U. Transverse instability and low-frequency flapping in incompressible separated boundary layer flows: an experimental study. *J. Fluid Mech.*, Vol. 703, pp. 363–373, 2012.
- [8] Rodríguez D, Gennaro E.M and Souza L.F. Self-excited primary and secondary instability of laminar separation bubbles. *J. Fluid Mech.*, Vol. 906, A13, 2021.
- [9] Karaca S and Gungor A.G. DNS of unsteady effects on the control of laminar separated boundary layers. *European Journal of Mechanics B/Fluids*, Vol. 56, pp. 71-81, 2016.
- [10] Marquillie M and Ehrenstein U. On the onset of nonlinear oscillations in a separating boundary-layer flow. *J. Fluid Mech.*, Vol. 490, pp. 169–188, 2003.
- [11] Saavedra J and Paniagua G. Transient performance of separated flows: characterization and active flow control. *J. Eng. Gas Turbines Power.*, Vol. 141(1), GTP-18-1311. 2019.
- [12] Saavedra J and Paniagua G. Experimental analysis of Reynolds effect on flow detachment and sudden flow release on a wall-mounted hump. *Exp. Thermal Fluid Science.*, Vol. 126, 110398. 2021.

- [13] Nordström, J., Nordin, N., and Henningson, D. The fringe region technique and the fourier method used in the direct numerical simulation of spatially evolving viscous flows. *SIAM J. Sci. Comput.*, Vol. 20, No. 4, pp. 1365-1393. 1999.
- [14] Ferrer et al. HORSES3D: a high-order discontinuous Galerkin solver for flow simulations and multi-physics applications. arXiv:2206.09733. 2022.
- [15] Hussain A.K.M.F, and Reynolds W.C. The mechanics of an organized wave in turbulent shear flow. *J. Fluid Mech.*, Vol. 41, part 2, pp. 241-258. 1970.
- [16] Avanci, M.P., Rodríguez, D. and Alves, L.S.B. A geometrical criterion for absolute instability in laminar separation bubbles. *Phys. Fluids*, Vol. 31, 014103. 2019.
- [17] Himeno F.H.T, Souza D.S, Amaral F.R, Rodríguez D, and Medeiros M.A.F. SPOD analysis of noise-generating Rossiter modes in a slat with and without a bulb seal. *J. Fluid Mech.*, Vol. 915, A67. 2021.